Journal of Power Sources 197 (2012) 285–291

Contents lists available at SciVerse ScienceDirect

Journal of Power Sources

journal homepage: www.elsevier.com/locate/jpowsour

Structural properties and electrochemistry of α-$LiFeO_2$

A.E. Abdel-Ghany[a,b], A. Mauger[c], H. Groult[b], K. Zaghib[d,*], C.M. Julien[b]

[a] Inorganic Chemistry Department, National Research Centre, Behoos Street, Dokki, Cairo, Egypt
[b] Laboratoire de Physicochimie des Electrolytes, Colloïdes et Systèmes Analytiques (PECSA) UMR 7195, Université Pierre et Marie Curie, Bat. F74, 4 place Jussieu, 75005 Paris, France
[c] Institut de Minéralogie et Physique de la Matière Condensée, Université Pierre et Marie Curie, 4 place Jussieu, 75005 Paris, France
[d] Institut de Recherche d'Hydro-Québec, 1800 Bd Lionel-Boulet, Varennes, Québec, Canada J3X 1S1

ARTICLE INFO

Article history:
Received 26 July 2011
Received in revised form
18 September 2011
Accepted 19 September 2011
Available online 29 September 2011

Keywords:
Lithium ferrite
Solid-state reaction
Li-ion batteries
Magnetic properties

ABSTRACT

In this work, we study the physico-chemistry and electrochemistry of lithium ferrite synthesized by solid-state reaction. Characterization included X-ray diffraction (XRD), scanning electronic microscopy (SEM), Raman scattering (RS), Fourier transform infrared spectroscopy (FTIR), and SQUID magnetometry. XRD peaks gradually sharpen with increasing firing temperature; all the diffraction peaks can be indexed to the cubic α-$LiFeO_2$ phase (*Fm3m* space group) with the refined cell parameter $a = 4.155$ Å. RS and FTIR spectra show the vibrational modes due to covalent Fe–O bonds and the Li-cage mode at low-frequency. The electrochemical properties of Li/$LiFeO_2$ are revisited along with the post-mortem analysis of the positive electrode material using XRD and Raman experiments.

1. Introduction

Various lithiated transition-metal dioxides $LiMO_2$ (M = Ni, Co, Mn) have been investigated as insertion compounds for potential used in rechargeable Li batteries [1–3]. Two decades ago, the discovery of the electrochemical features of $LiCoO_2$ as a positive electrode material has lead a great progress for energy storage devices followed by extensive researches on alternative, inexpensive, thermally safe and environmentally friendly materials. In this context, Goodenough and Kim [3] have recently discussed the strategies for Li-ion batteries that are based on lithium-intercalation compounds as electrodes because limitations are due to the capacity of a cathode material and the safe charging rates for Li transport across the passivating SEI layer on a carbon-based anode.

Varieties of $LiFeO_2$ (LFO) have been studied as potential alternatives to Li–Co–O positive electrodes. Depending on the precursors and the synthetic methods used, LFOs exhibit various crystalline polymorphs [4–29]. A classification has been proposed by Kanno et al. [8]. The cation-disordered α-$LiFeO_2$ phase has a cubic structure of *Fm3m* space group (SG) [10–12], the cation-ordered γ-$LiFeO_2$ has a tetragonal structure ($I4_1/amd$ SG) by ordering the Li^+ and Fe^{3+} ions at octahedral sites [10], β-$LiFeO_2$ noted β′-, β*- and β″-phase are intermediate phases [13]. Other forms include the corrugated layer $LiFeO_2$ structure similar to γ-FeOOH (orthorhombic, *Pnma* SG) [16–22], the goethite-type structure similar to α-FeOOH [22], the hollandite-type $LiFeO_2$ structure similar to β-FeOOH [23], and non-stoichiometric compounds with mixed structures [24–26]. The orthorhombic form, o-$LiFeO_2$, was synthesized at low temperature [21]. Recently, the layered O3-$LiFeO_2$ structure (α-$NaFeO_2$-type, hexagonal, *R-3m* SG) has been synthesized by an ion-exchange reaction with α-$NaFeO_2$ [14–16].

Among the isomers, α-$LiFeO_2$ crystallizes in a NaCl type structure, in which Li and Fe atoms occupy randomly the octahedral sites in a cubic close packing of oxygen atoms as shown in Fig. 1.One major drawback of lithium ferrites as electrode materials results from their low cycling efficiency and low operating voltage [12,16–22,27]. However, for some Li–Fe–O systems, similar initial capacities to those of $LiCoO_2$ and $LiFePO_4$ have been obtained [21,29]

The focus of this work is the study of the α-$LiFeO_2$ form synthesized by the classical ceramic method from selected iron oxide and lithium carbonate as raw materials. The material is structurally characterized by a set of experiments including X-ray diffraction, scanning electron microscopy, optical spectroscopy (FTIR and Raman) and magnetometry. The electrochemical properties of Li/$LiFeO_2$ cell are revisited along with the post-mortem analysis of the positive electrode material.

2. Experimental

The lithium ferrite powders were synthesized by the solid-state reaction (ceramic) method using selected iron oxide (Fe_2O_3) and lithium carbonate (Li_2CO_3) as raw materials taking a small excess

* Corresponding author. Tel.: +1 450 652 8019; fax: +1 450 652 8424.
E-mail address: zaghib.karim@ireq.ca (K. Zaghib).

0378-7753/$ – see front matter © 2011 Elsevier B.V. All rights reserved.
doi:10.1016/j.jpowsour.2011.09.054

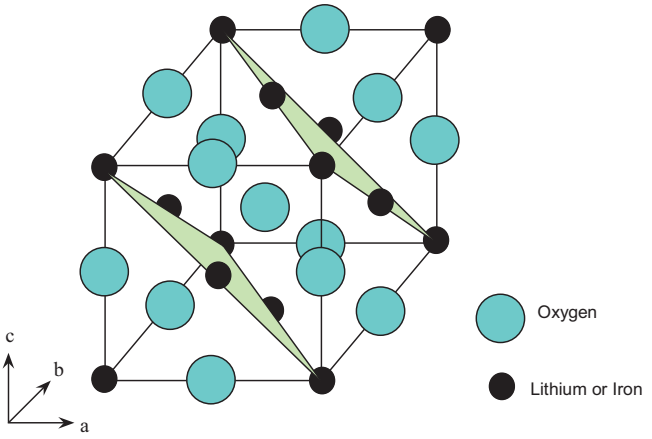

Fig. 1. Schematic representation of the crystal structure of α-$LiFeO_2$.

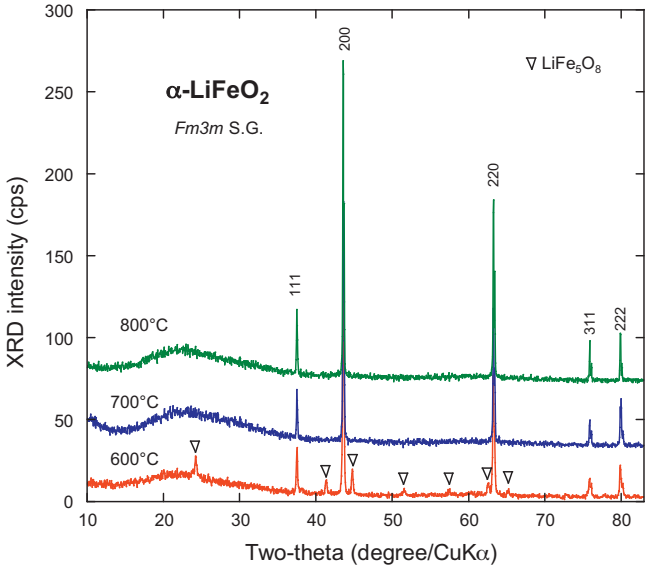

Fig. 2. XRD pattern of α-$LiFeO_2$ prepared by solid-state reaction using Fe_2O_3 and Li_2CO_3 raw materials. Powders were calcined at (a) 600 °C, (b) 700 °C and (c) 800 °C under argon flow.

of lithium (Li:Fe > 1). The starting materials was finely ground in a mortar and placed in a tube furnace for heat treatment at different temperatures in the range 400–800 °C for 12 h in an argon atmosphere. Several intermittent grindings were performed between the steps of calcination. The crystalline phase was identified by X-ray diffraction (XRD) using Philips X'Pert apparatus equipped with a CuK_α X-ray source ($\lambda = 1.5406$ Å). XRD measurements were collected in the 2θ range 10–80° at slow scan rate of 0.001° min^{-1}. The particle morphology of the $LiFeO_2$ powders was examined with a scanning electron microscope (SEM, JEOL-Japan, JXA-840A).

Infrared absorption spectra were recorded at room temperature using a Fourier transform interferometer (Bruker IFS113v) interferometer at a spectral resolution 2 cm^{-1}. In the studied region (100–1000 cm^{-1}), this vacuum bench apparatus was equipped with 3.5 μm-thick mylar and Ge/KBr beam splitter, a global source, and a DTGS/PE far-infrared detector. Samples were ground to fine powders and dispersed into ICs pellets in the 1:300 proportion. Raman spectra were collected with a Jobin-Yvon U1000 double-pass spectrometer equipped with a cooled, low noise photomultiplier tube (ITT FW130). The excitation light was the 515 nm Ar^+-laser line. Raman and FTIR spectra were fitted using the curve analysis based on the original algorithm of non-linear peak fitting known as the Levenberg–Marquardt method. The fitting calculation of IR spectra was done assuming a linear baseline in the spectral range 150–1000 cm^{-1} using OPUS package from Bruker GmbH. All the Raman bands introduced in the fit had a Lorentzian lineshape; two adjusting parameters (intensity and band-width) were considered for each Lorentzian oscillator.

Magnetic measurements (susceptibility and magnetization) were carried out in the range 0–30 kOe using a fully automated magnetometer (MPMS-5S from Quantum Design) using an ultra-sensitive Superconducting Quantum Interference Device (SQUID) in the temperature range 4–300 K. Powders were placed into a small plastic vial, placed in a holder and finally inserted into the helium Dewar flask of the SQUID apparatus. The temperature dependence of the susceptibility data was recorded during heating of the sample using two modes: zero field cooling (ZFC) and field cooling (FC), to determine the magnetic behavior. The procedure is based on performing two consecutive magnetization measurements: in ZFC the sample is first cooled down in the absence of magnetic field, then a magnetic field $H = 10$ kOe are applied, and the ZFC magnetic susceptibility $M(T)/H$, where M is the magnetization measured upon heating. In the FC experiments, the same magnetic field is applied first at room temperature; the FC susceptibility is measured upon cooling.

The electrochemical properties of LNMCO were tested at room temperature in cells with metallic lithium as anode electrode. The electrolyte solution was 1 mol L^{-1} $LiPF_6$ in a mixture of ethylene carbonate (EC) and dimethyl carbonate (DMC) in a 1:1 volume ratio. A Celgard microporous polypropylene membrane was used as a separator. The positive electrode was prepared by mixing the active material with acetylene black and binder (polyvinylidene fluoride, PVDF, dissolved in *N*-methyl-2-pyrrolidone, NMP) in a weigh ratio of 80:10:10. The mixture was pressed onto stainless steel mesh used as current collector and dried under vacuum at 80 °C for 16 h. The laboratory cells were assembled in an argon-filled glove box. The charge and discharge profiles were collected by galvanostatic cycling between 1.5 and 4.4 V vs. Li^0/Li^+, applying a constant current of *C*/12 rate at room temperature with a Mac-Pile battery testing system (160 mA g^{-1} was assumed to be 1*C*-rate).

3. Results and discussion

3.1. Structure and morphology

Fig. 2 shows the XRD patterns of the synthesized LFO materials synthesized by the ceramic route with sintering at different temperatures T_s. The XRD peaks are getting thinner and more intense upon increasing T_s, which indicates the best crystallinity is achieved for the sintering temperature $T_s = 800$ °C. A close examination of the XRD diagrams of powders sintered at $T_s < 700$ °C indicates the presence of impurity phase attributed to $LiFe_5O_8$. Structurally, this lithium ferrite is an inverse spinel network in which Li^+ and Fe^{3+} ions occupied the octahedral B-sites. It is remarkably seen that the impurity-free α-$LiFeO_2$ has not been formed until heated above 600 °C, which exhibits a mixture of $LiFe_5O_8$ spinel and α-$LiFeO_2$ phases; also the presence of the β-$LiFeO_2$ form is not observed as reported by Tabuchi et al. [18]. Collongues and Chaudron concluded that $LiFeO_2$ and $LiFe_5O_8$ are the limiting members of the solid solutions formed by the replacement of $2Fe^{2+}$ by $Li+Fe^{3+}$ in 2FeO or $2Fe_3O_4$, respectively [30].

For the optimum sintering temperature $T_s \approx 800$ °C) and a small excess of lithium in the starting mixture (Li:Fe ≈ 1.15), the XRD spectrum are in agreement with those reported in the literature for α-$LiFeO_2$ [11,12]. It is well indexed in the *Fm3m* symmetry of the NaCl-like cubic structure without contamination. The lattice parameter of the cubic structure we thus obtain is $a = 4.155$ Å,

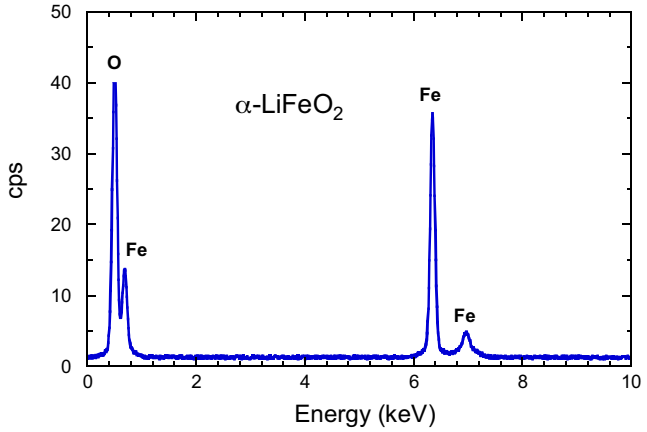

Fig. 3. EDAX elemental analysis of the $LiFeO_2$ sample annealed at 800 °C.

matches well with the given value (JCPDS 74-2283) and previous literature reports as well [11,28].

As seen in Fig. 2, the XRD pattern is dominated by the (2 0 0) Bragg line (strongest intensity) at $2\theta = 43.59°$ and the (1 1 1) and (2 2 0) lines (medium intensity) at $2\theta = 37.45$ and 63.29°, respectively. The narrow diffraction peaks of the pattern indicate a high crystallinity of the LFO powder. The coherence length, L_c, has been estimated using Scherrer formula:

$$L_c = \frac{K \times \lambda}{\beta \times \cos\theta} \quad (1)$$

where β is the full width at half maximum (FWHM) in radians, the constant is $K = 0.9$, λ is the wavelength of the X-ray, θ is the corresponding Bragg angle. We find $L_c = 52 \pm 5$ nm that corresponds to the particle size, L, estimated from the SEM images (see below).

EDX experiments were used for the chemical analysis of the sample prepared with the ratio Li:Fe = 1.15. The EDX spectrum (Fig. 3) exhibits the characteristic peaks of Fe and O present in the sample. It is not possible to detect Li for the obvious reason that the X-ray fluorescence yield is extremely low for elements such as Li or Be. The respective peaks due to Fe and O are indicated along with their respective energy positions. The lines identified are O $K\alpha_1$, Fe Kα and Fe Lβ, respectively. The presence of peaks due to other elements as either dopants or impurities is not detected, which is an indication of the sample chemical purity.

The degree of crystallinity of the $LiFeO_2$ product, i.e. domain size, grain distribution, was examined by SEM experiments. Fig. 4(a and b) shows the typical scanning micrograph of a sample fired at 650 and 800 °C, respectively. These pictures reveal that particles fired at 800 °C have regular spherical-like shape with an average diameter of 0.55 μm and a fairly narrow particle size distribution range. The quasi-spherical shape of the particles is attributed to the careful synthesis of the product including extensive grinding between successive calcinations. It should be noted that the values of mean coherence length (≈52 nm) obtained from XRD analysis according to Scherrer formula is about one order of magnitude smaller than the dimensions of the primary particles, so that the primary particles should not be confused with crystallites. The SEM pictures display the absence of agglomerates and ensure the high specific surface area of samples.

3.2. Vibrational spectra

The purpose of this study is to investigate the local environment of cations in a cubic-close-packed oxygen array of the $LiFeO_2$ lattice using vibrational spectroscopy. IR- and Raman-active modes correspond to vibrations involving primarily atomic motion of cations against their oxygen neighbors. Consequently, these modes are very sensitive to the cationic local environment in the host matrix which can be affected by cationic distribution, cation mixing, disorder, etc.

Fig. 5 shows the FTIR absorption spectrum of $LiFeO_2$ sample fired at 800 °C in argon atmosphere. The FTIR features are dominated by a broad band centered at ca. 380 cm^{-1} that originates from the cubic NaCl-type structure of α-$LiFeO_2$. The best fit of the FTIR spectrum has been achieved using eight bands at 242, 344, 383, 436, 508, 566, 688 and 864 cm^{-1} that correspond to the F_{1u} modes of the *Fm3m* symmetry.

Fig. 6 displays the Raman spectrum of $LiFeO_2$, which is characterized by the occurrence of five bands at 256, 533, 577, 646 and 704 cm^{-1}, that belong to the species $F_{1g}+F_{2g}$. The strongest peaks located at 533 and 646 cm^{-1} are attributed to the O–Fe–O bending and the Fe–O stretching mode of FeO_6 octahedra, while the mode at low frequency, at ca. 256 cm^{-1}, is assigned to the Li-cage in an octahedral environment. Similar features have been observed in spectra of $LiMO_2$ (M = Ni, Co, Cr) materials [31]. In particular, the Li-cage mode in the same O_h configuration has been observed at 260 cm^{-1} in $LiCoO_2$, 240 cm^{-1} in $LiNiO_2$. The line at 256 cm^{-1} in α-$LiFeO_2$ shifted by a few cm^{-1} with respect to $LiCoO_2$, corresponds to this same cage mode of the lithium ions which undergo translation vibrations inside the cage formed by the six nearest neighbor oxygen atoms.

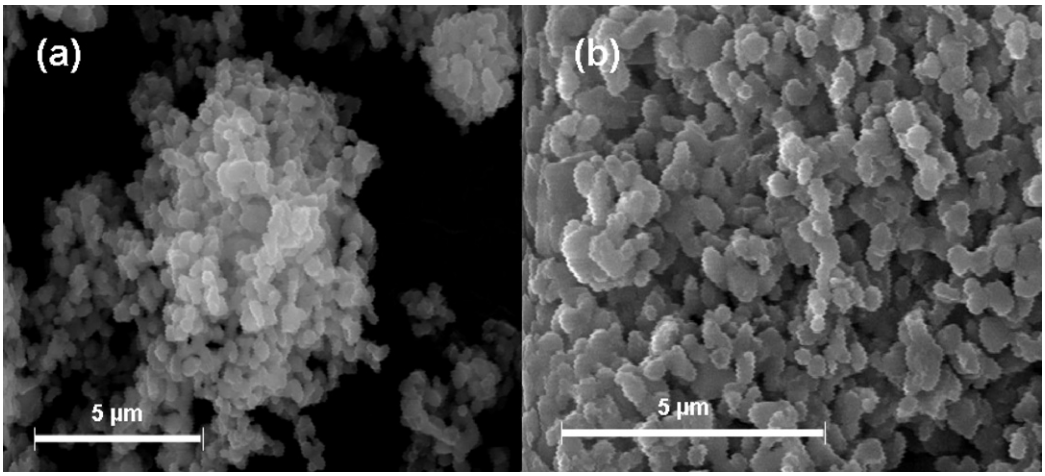

Fig. 4. Typical SEM micrographs of $LiFeO_2$ powders annealed at (a) 650 °C and (b) 800 °C in argon atmosphere. The spherical-like shape of particles is attributed to the grinding process.

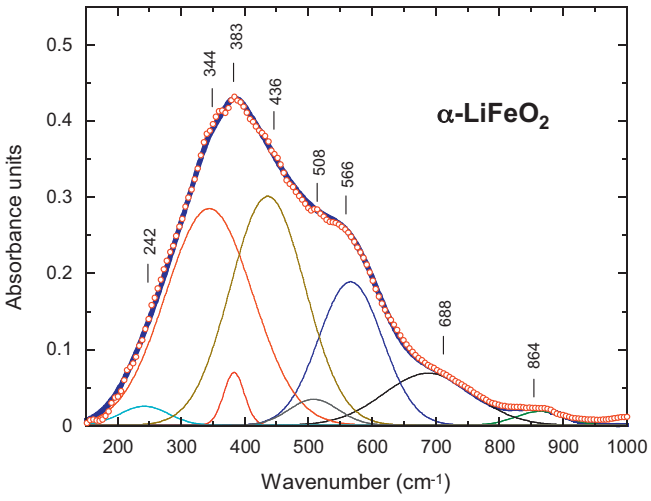

Fig. 5. FTIR absorption spectrum of $LiFeO_2$ prepared at 800 °C. The synthesized spectrum (full line) was obtained by a non-linear curve-fitting technique using the superposition of Gaussian–Lorentzian bands.

3.3. Magnetic properties of α-$LiFeO_2$

The magnetization curves of α-$LiFeO_2$ powders fired at 800 °C are reported in Fig. 7. The magnetization M is linear in the magnetic field H, down to $T = 50$ K. This result gives evidence that the $LiFe_5O_8$ or Fe_3O_4 impurities that are often present in $LiFeO_2$ [10,32] is absent in our samples. As a consequence, the magnetic susceptibility is simply given by <!– no-mfc –>$\chi = M/H$<!– /no-mfc –>. The $\chi^{-1}(T)$ curves measured at $H = 10$ kOe are reported in Fig. 8. The experimental curve shows a negative curvature instead of the linear behavior expected for the Curie–Weiss law. If we take the tangent to the experimental curve near room temperature to analyze the results according to the Curie–Weiss law,

$$\chi_m = \frac{N_A p_{eff}^2 \mu_B^2}{3k_B} \frac{1}{T + \theta_p}, \quad (2)$$

where the first fraction is the Curie constant C_p, N_A is the Avogadro number, k_B the Boltzman constant, p_{eff} the effective magnetic moment, μ_B the Bohr magneton and θ_p is the Curie–Weiss temperature. We find $\mu_{eff} = 4.94\ \mu_B$ and $\theta_p = -260$ K. The effective magnetic

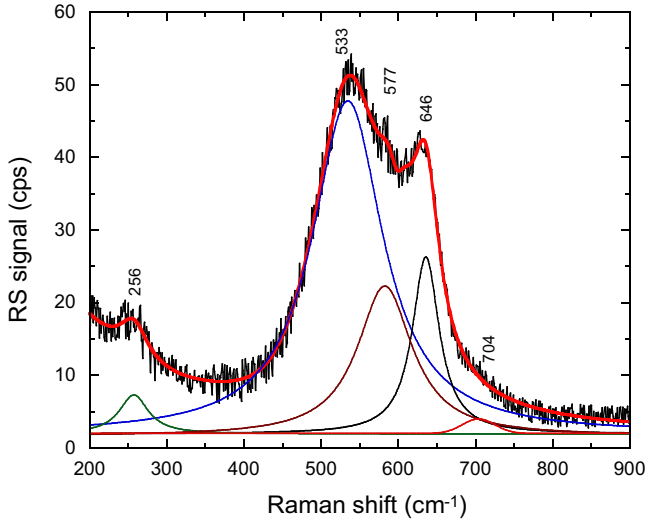

Fig. 6. Raman scattering spectrum of $LiFeO_2$ fired at 800 °C. The best fit to the Raman features has been achieved, starting from a prescribed set of individual bands of Lorentzian shape for the overlapping band profile.

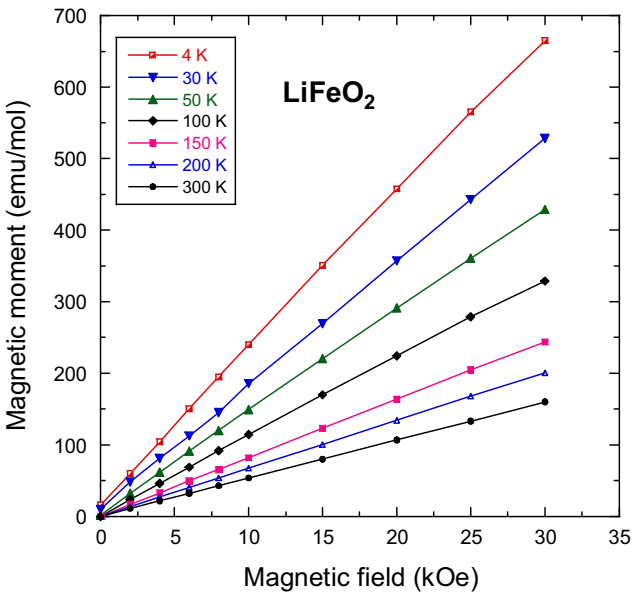

Fig. 7. Magnetization curve $M(H)$ as a function of the temperature for α-$LiFeO_2$ crystalline powders.

moment μ_{eff} carried by Fe ions is significantly smaller than the value 5.9 μ_B expected for Fe^{3+}. There is no doubt, however, that iron is trivalent. This has been evidenced for instance by Mössbauer spectroscopy in Ref. [10]. Iron ions can carry a magnetic moment smaller than that expected occasionally, but only in case of unsaturated covalent bonding, a situation met in Heusler alloys [33] or in other iron compounds [34,35]. The smaller value of μ_{eff} in our analysis is thus simply the evidence that the Curie–Weiss behavior can be observed only at temperatures that cannot be accessed in our experimental set-up. Indeed, it has been observed at higher temperature (up to 450 K), from which the value $\mu_{eff} = 5.9\ \mu_B$ has been recovered [32]. The antiferromagnetic ordering is best evidenced by the anomaly in the $\chi^{-1}(T)$ curve at the Néel temperature $T_N \cong 85$ K. This is consistent with the ^{57}Fe Mössbauer spectrum of α-$LiFeO_2$ at 77 K, showing the apparition of the sextet [10]. The

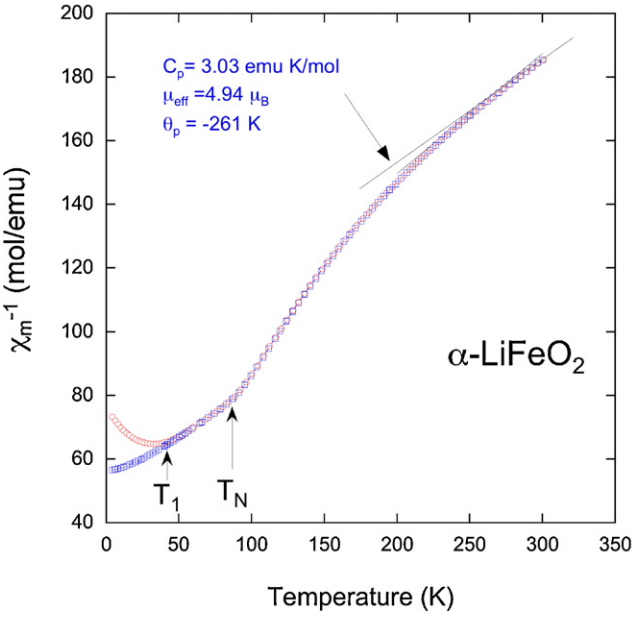

Fig. 8. Temperature dependence of the inverse molar magnetic susceptibility χ of α-$LiFeO_2$ powders for field cooled and zero-field cooled experiments.

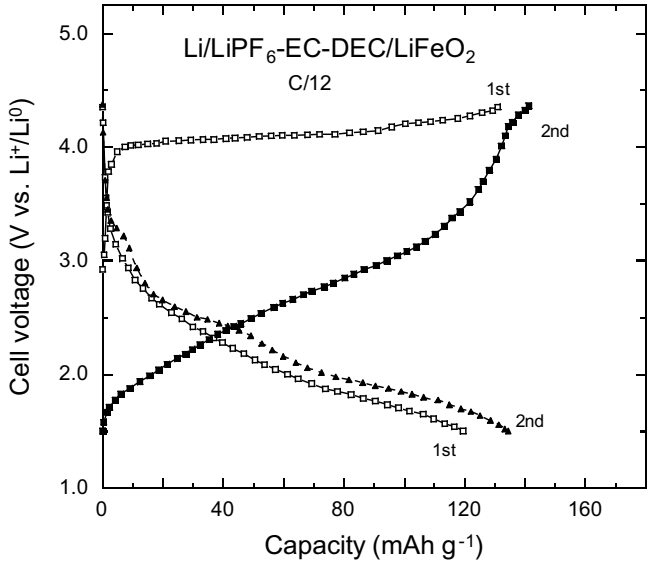

Fig. 9. Charge and discharge curves for the Li/$LiFeO_2$ cell with 1 mol L^{-1} $LiPF_6$-EC:DMC (1:1) electrolyte. The cell was cycled at current density mA g^{-1} (*C*/12) in the potential range 1.5–4.4 V.

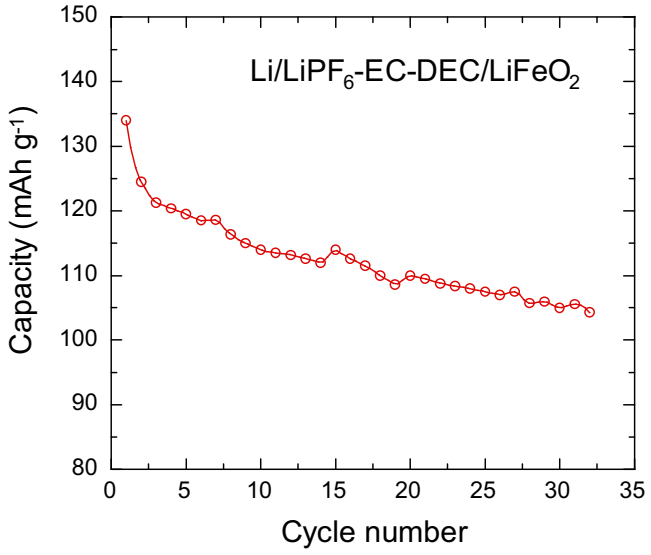

Fig. 11. Cycle number dependence of the discharge capacity for the Li/$LiFeO_2$ cell operating at *C*/12 in the potential range 1.5–4.4 V.

onset of magnetic irreversibility takes place at $T_1 \cong 40$ K, and is evidenced in Fig. 8 by a separation between the zero-field cooled (ZFC) and field-cooled (FC) susceptibility curves. This is another feature of Fe-diluted magnetic semiconductors [35,36].

3.4. Electrochemical studies

Fig. 9 shows the charge and discharge curves of the Li/$LiFeO_2$ cell for the first and second cycles with a constant current density of 13.5 mA g^{-1} (*C*/12 rate) between 1.5 and 4.4 V versus Li^0/Li^+ at room temperature. The first charge process displays a voltage plateau at 4.1 V; it disappeared in the second charge. The subsequent charge process shows an S-shape curve observed in the 3-V region, while the discharge curve exhibits two plateaus around 2.54 and 1.91 V. These results are well seen on the incremental capacity d*Q*/d*V* vs. cell voltage curve (Fig. 10), in which the peaks correspond to plateau in Fig. 10. It is remarked that similar features were observed for Li/LFO cells including positive electrode with different structures such as the corrugated layer $LiFeO_2$ [22], the layered O3-$LiFeO_2$ [29], the hollandite-like tunnel structure [23] and the o-$LiFeO_2$ structure [20]. However, the value of the voltage plateaus appeared structure dependent. The existence of two plateaus (or two peaks in Fig. 10) suggests two different sites for Li. Though Li^+ and Fe^{3+} occupy the octahedral sites randomly, a short-range order is needed to satisfy the Pauling's electrostatic rule [37]. Eight corners of a given octahedron are always occupied by four Li^+ ions and four Fe^{3+} ions, but two types of arrangement are possible [38]. They have been observed experimentally by TEM experiments [41]. We find here their indirect observation by electrochemistry, since these two local arrangements also mean the two non-equivalent Li sites revealed in Figs. 10 and 11. Note also that it also implies two non equivalent Fe^{3+} sites, and the absence of infinitely long range antiferromagnetic ordering at T_N discussed in the previous section may also be linked to this phenomenon, as it played also this role in another Fe-based compound [35].

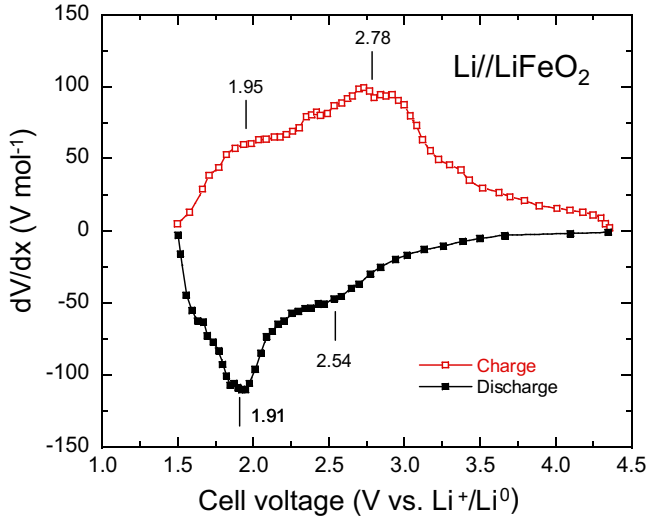

Fig. 10. Incremental capacity d*Q*/d*V* vs. cell potential obtained at the second cycle for $LiFeO_2$ fired at 800 °C.

The charge and discharge curves in the subsequent cycles differ from those in the first cycle. Morales et al. [39] have shown that iron (III) is oxidized to iron (IV) during charge and reduced to iron (II) during the first discharge. Sakurai et al. have pointed out that unusual Fe^{4+} ions generated during the first charge could play a role in the voltage hysteresis of $LiFeO_2$ [40]. It is believed that Fe^{4+} ions are formed during the reaction which takes place at the electrode.

$$LiFeO_2 - xLi^+ - xe^- \rightarrow Li_{1-x}Fe^{III}_{1-x}Fe^{IV}_xO_2 \quad (3)$$

with a displacement from octahedral 4*a* to tetrahedral 8*c* positions, while Li^+ ions remained in 8*c* sites insuring a conduction pathway [41]. From electrochemical features shown in Fig. 9 we observed a capacity loss of 15 mAh g^{-1} between the first and second cycle. Fig. 11 shows the discharge capacity of Li/$LiFeO_2$ cell. It is shown that the capacity decreases continuously upon cycling to reach the value 104 mAh g^{-1} for the 32nd cycle.

3.5. Post-mortem studies

As we observed in Fig. 9 big changes occurred upon charge–discharge process for the Li/α-$LiFeO_2$ cell; the focus of this section is the study of the structural changes after the first charge and after five cycles within a voltage range between 1.5 and 4.4 V. In order to investigate these modifications the electrode was investigated by ex situ XRD and Raman measurements. The electrodes

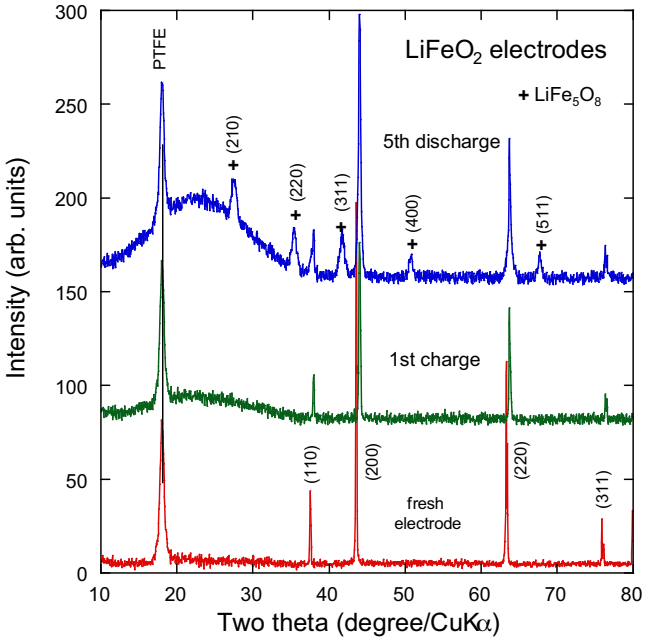

Fig. 12. Post-mortem XRD patterns of $LiFeO_2$ electrodes: (a) pristine, (b) charged electrode at the first cycle, and (c) discharged electrode at the 5th cycle. The electrodes were washed with DMC solution to remove $LiPF_6$ salt.

were washed with DMC solution to remove $LiPF_6$ salt and left in a glove box for 12 h to reach equilibrium. Fig. 12 shows the structural change of α-$LiFeO_2$ after the fresh cell being charged at 4.4 V. A shift of $LiFeO_2$ Bragg lines toward higher angles is observed that corresponds to a small decrease of the cubic cell parameter. At the end of the 5th charge–discharge process, the XRD peaks broaden and a new phase has grown. The XRD spectrum shows the occurrence of the $LiFe_5O_8$ spinel identified by the lines (2 1 0), (2 2 0), (3 1 1) and (4 0 0).

In order to confirm the remained phase in the electrode after charge and discharge reaction, the Raman scattering spectra have been recorded on the same samples examined by XRD. Fig. 13 displays such spectra. At the first charge the Raman features consist in the spectrum of α-$LiFeO_2$ shifted toward the low wavenumber side, which indicates a strengthening of the Fe–O chemical bonds. At the end of the 5th cycle, the RS spectrum shows clearly the superposition of two components, α-$LiFeO_2$ plus $LiFe_5O_8$ similarly to the XRD patterns. The strong Fe–O stretching mode of $LiFe_5O_8$ is recorded at 720 cm^{-1}.

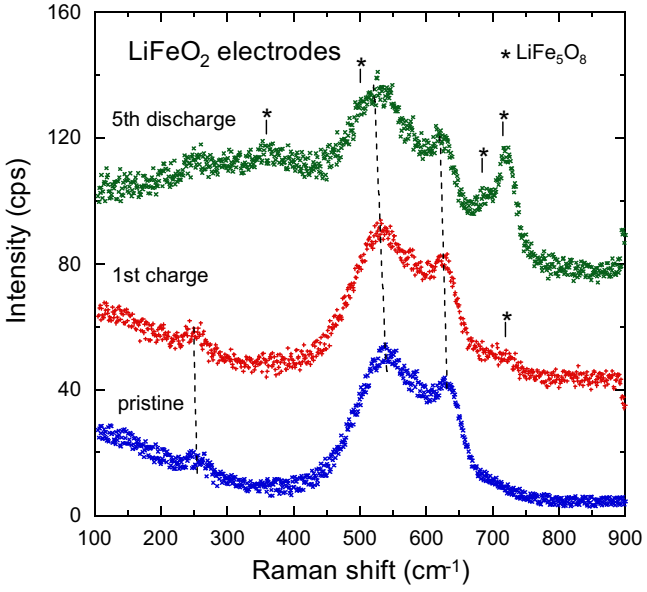

Fig. 13. Post-mortem Raman scattering spectra of $LiFeO_2$ electrodes: (a) pristine, (b) charged electrode at the first cycle, and (c) discharged electrode at the 5th cycle. The electrodes were washed with DMC solution to remove $LiPF_6$ salt.

Similar structural modifications have been reported previously for several LFO polymorphs such as the orthorhombic o-$LiFeO_2$ [20] and the layered O3-$LiFeO_2$ [29]. For o-$LiFeO_2$, severe structural changes occurred during the first charge–discharge process of the cells, i.e. from orthorhombic to spinel phase, which induces the capacity loss of the Li/$LiFeO_2$ system. A TEM analysis revealed clearly that the spinel $LiFeO_2$ phase was found in the electrode after the 3rd cycle and the total structural transformation was completed after 50 cycles [20]. In the case of O3-$LiFeO_2$, Mössbauer measurements revealed that the oxidation state of iron (Fe^{3+}) did not change but a phase transition from rhombohedral to cubic symmetry occurred during the initial charge, indicating oxygen release with lithium deinsertion [29].

4. Conclusion

Crystallo-chemistry of lithium iron oxide $LiFeO_2$ has shown that, this compound crystallizes in the cubic structure (*Fm*3*m* SG). $LiFeO_2$ sample synthesized via solid-state reaction exhibits well-formed crystallites of 0.55 μm size. A combination of FTIR and RS measurements confirms the cubic structure of $LiFeO_2$. Magnetic measurements have evidence that α-$LiFeO_2$ exhibits deviation from the Curie–Weiss law with $\mu_{eff} \ll 5.9\,\mu_B$ at room temperature. The cationic disorder seems to affect the magnetic properties. This compound is expected to belong to the class of Fe-diluted magnetic semiconductors regarding its magnetic properties. Electrochemical texts show severe structural changes that occurred during the first charge–discharge process of the cells. The structural transformation from α-$LiFeO_2$ to $LiFe_5O_8$ spinel phase has been evidenced by ex situ X-ray diffraction and Raman spectroscopy.

References

[1] K. Mizushima, P.C. Jones, P.J. Wiseman, J.B. Goodenough, Mater. Res. Bull. 15 (1980) 783.
[2] C.D.W. Jones, E. Rosen, J.R. Dahn, Solid State Ionics 68 (1994) 65.
[3] G.B. Goodenough, Y. Kim, J. Power Sources 196 (2011) 6688.
[4] M. Brunel, F. de Bergevin, J. Phys. Chem. Solids 29 (1968) 163.
[5] R. Famery, P. Bassoul, F. Queyroux, J. Solid State Chem. 57 (1985) 178.
[6] R. Famery, P. Bassoul, F. Queyroux, J. Solid State Chem. 61 (1986) 293.
[7] B. Fuchs, S. Kemmler-Sack, Solid State Ionics 68 (1994) 279.
[8] R. Kanno, T. Shirane, Y. Kawamoto, Y. Takeda, M. Takana, M. Ohashi, Y. Yamaguchi, J. Electrochem. Soc. 143 (1996) 2435.
[9] K. Ado, M. Tabuchi, H. Kobayashi, H. Kageyama, O. Nakamura, Y. Inaba, R. Kanno, M. Takagi, Y. Takeda, J. Electrochem. Soc. 144 (1997) L177.
[10] M. Tabuchi, S. Tsutsui, C. Masquelier, R. Kanno, K. Ado, I. Matsubara, S. Nasu, H. Kageyama, J. Solid State Chem. 140 (1998) 159.
[11] Y. Sakurai, H. Arai, J.-I. Yamaki, Solid State Ionics 113–115 (1998) 29.
[12] X. Wang, L. Gao, F. Zhou, Z. Zhang, M. Ji, C. Tang, T. Shen, H. Zeng, J. Cryst. Growth 265 (2004) 220.
[13] R. Akiyama, Y. Ikedo, M. Mansson, T. Goko, J. Sugiyama, D. Andreica, A. Amato, K. Matan, T.J. Sato, Phys. Rev. B 81 (2010) 024404.
[14] T. Shirane, R. Kanno, Y. Kawamoto, Y. Takeda, M. Takano, T. Kamiyama, F. Izumi, Solid State Ionics 79 (1995) 227.
[15] M. Tabuchi, C. Masquelier, T. Takeuchi, K. Ado, I. Matsubara, T. Shirane, R. Kanno, S. Tsutsui, S. Nasu, H. Sakaebe, O. Nakamura, Solid State Ionics 90 (1996) 129.
[16] R. Kanno, T. Shirane, Y. Inaba, Y. Kawamoto, J. Power Sources 68 (1997) 145.
[17] R. Kanno, T. Shirane, Y. Kawamoto, Y. Takeda, M. Takano, M. Ohashi, Y. Yamaguchi, J. Electrochem. Soc. 143 (1996) 2435.
[18] M. Tabuchi, K. Ado, H. Sakaebe, C. Masquelier, H. Kageyama, O. Nakamura, Solid State Ionics 79 (1995) 220.
[19] Y.S. Lee, C.S. Yoon, Y.K. Sun, K. Kobayakawa, Y. Sato, Electrochem. Commun. 4 (2002) 727.
[20] Y.S. Lee, S. Sato, M. Tabuchi, C.S. Yoon, Y.K. Sun, K. Kobayakawa, Y. Sato, Electrochem. Commun. 5 (2003) 549.
[21] Y.S. Lee, S. Sato, Y.K. Sun, K. Kobayakawa, Y. Sato, J. Power Sources 119–121 (2003) 285.

[22] Y. Sakurai, H. Arai, S. Okada, J.-I. Yamaki, J. Power Sources 68 (1997) 711.
[23] T. Matsumura, R. Kanno, Y. Inaba, Y. Kawamoto, M. Takano, J. Electrochem. Soc. 149 (2002) A1509.
[24] J. Kim, A. Manthiram, J. Electrochem. Soc. 146 (1999) 4371.
[25] Z. Han, X. Chen, W. Zhang, C. Zhong, H. Zhao, Y. Qian, Mater. Chem. Phys. 69 (2001) 292.
[26] Y.T. Lee, C.S. Yoon, Y.S. Lee, Y.-K. Sun, J. Power Sources 134 (2004) 88.
[27] Y. Sakurai, H. Arai, J. Yamaki, Solid State Ionics 113–115 (1998) 29.
[28] M. Tabuchi, A. Nakashima, H. Shigemura, K. Ado, H. Kobayashi, H. Sakaebe, K. Tatsumi, H. Kageyama, T. Nakamura, R. Kanno, J. Mater. Chem. 13 (2003) 1747.
[29] M. Hirayama, H. Tomita, K. Kubota, R. Kanno, J. Power Sources 196 (2011) 6809.
[30] R. Collongues, G. Chaudron, Compt. Rend. Acad. Sci. (Paris) 124 (1950) 143.
[31] C.M. Julien, Solid State Ionics 136 (2000) 887.
[32] J.C. Anderson, S.K. Dey, V. Halpern, J. Phys. Chem. Solids 26 (1965) 1555.
[33] J. Kübler, A.R. Williams, C.B. Sommers, Phys. Rev. B 28 (2003) 1745.
[34] R. Viennois, D. Ravot, J.C. Tedenac, S. Charar, A. Mauger, Mater. Sci. Eng. B 119 (2005) 1.
[35] P. Amornpitoksuk, D. Ravot, A. Mauger, J.C. Tedenac, Phys. Rev. B 77 (2008) 144405.
[36] A. Mauger, D. Ravot, P. Bonville, P. Solokha, S. De Negri, V. Pavlyuk, A. Saccone, J.-C. Tedenac, J. Alloys Compd. 508 (2010) 28.
[37] L. Pauling, The Nature of the Chemical Bond, 3rd ed., Cornell University Press, Ithaca, 1960, pp. 547.
[38] K. Kohiki, K. Hori, K. Ogawa, H. Shimooka, T. Tajiri, H. Deguchi, M. Mitome, Y. Bando, Jpn. J. Appl. Phys 43 (2004) L1232.
[39] J. Morales, J. Santos-Pena, R. Trocoli, S. Franger, Electrochim. Acta 53 (2008) 6366.
[40] Y. Sakurai, H. Arai, S. Okada, J. Yamaki, J. Power Sources 68 (1998) 711.
[41] A.R. West, Basic Solid State Chemistry, 2nd ed., Wiley, New York, 1999.